Supplementary Material for

# Achieving persistent and ultra-high voltage output through arid-adapted plants-inspired high-performance moisture-electric generator

Yu Chen,[a] Chengwei Ye,[a] Jiajun He,[a] Rui Guo,[a] Liangti Qu,*[,b] Shaochun Tang*[, a]

[a] *National Laboratory of Solid State Microstructures, Collaborative Innovation Center of Advanced Microstructures, Jiangsu Key Laboratory of Artificial Functional Materials, College of Engineering and Applied Sciences, Nanjing University, Nanjing 210093, P. R. China.*

[b] *Key Laboratory of Organic Optoelectronics & Molecular Engineering, Ministry of Education, Department of Chemistry, Tsinghua University, Beijing, 100084 P. R. China*

Corresponding authors *E-mails: lqu@mail.tsinghua.edu.cn; tangsc@nju.edu.cn

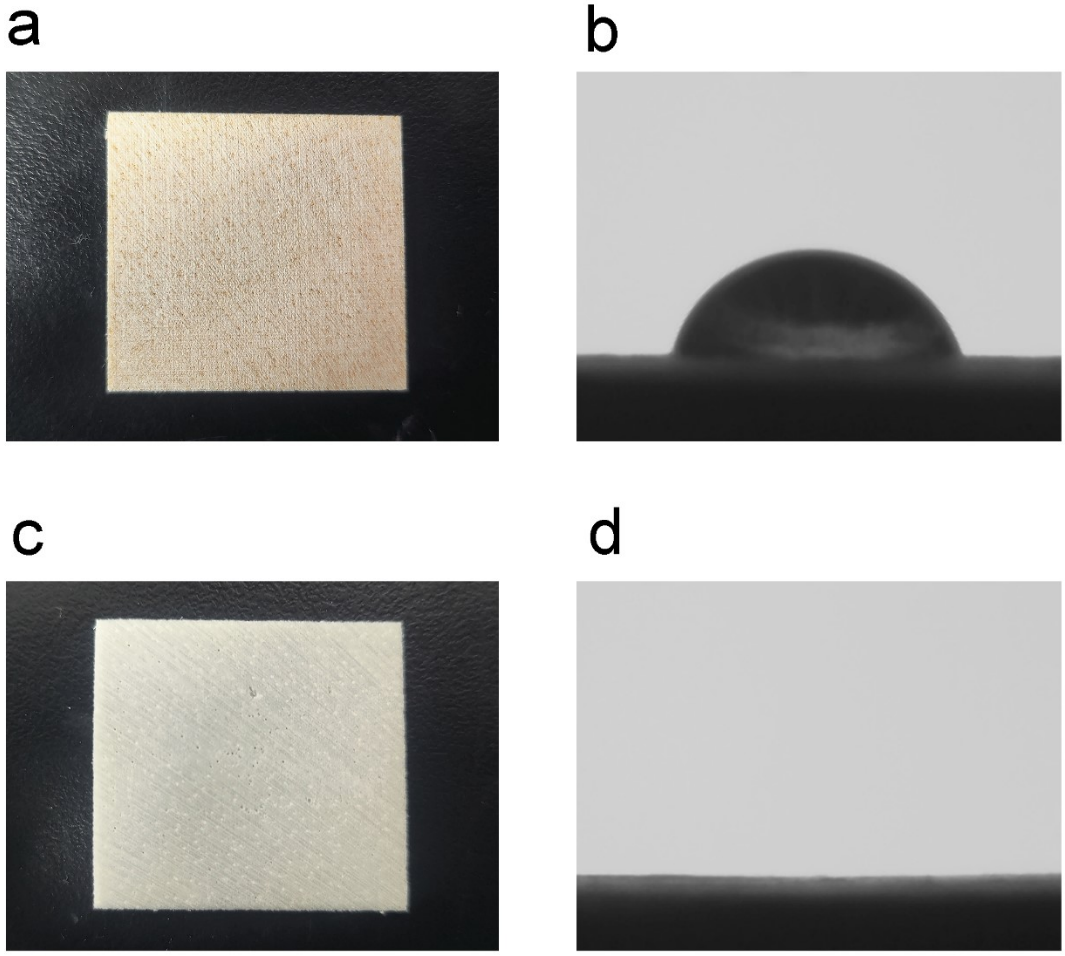


**Figure S1**. Optical photographs and contact angle photographs of raw wood (**a**, **b**) before, and (**c**, **d**) after delignification treatment.

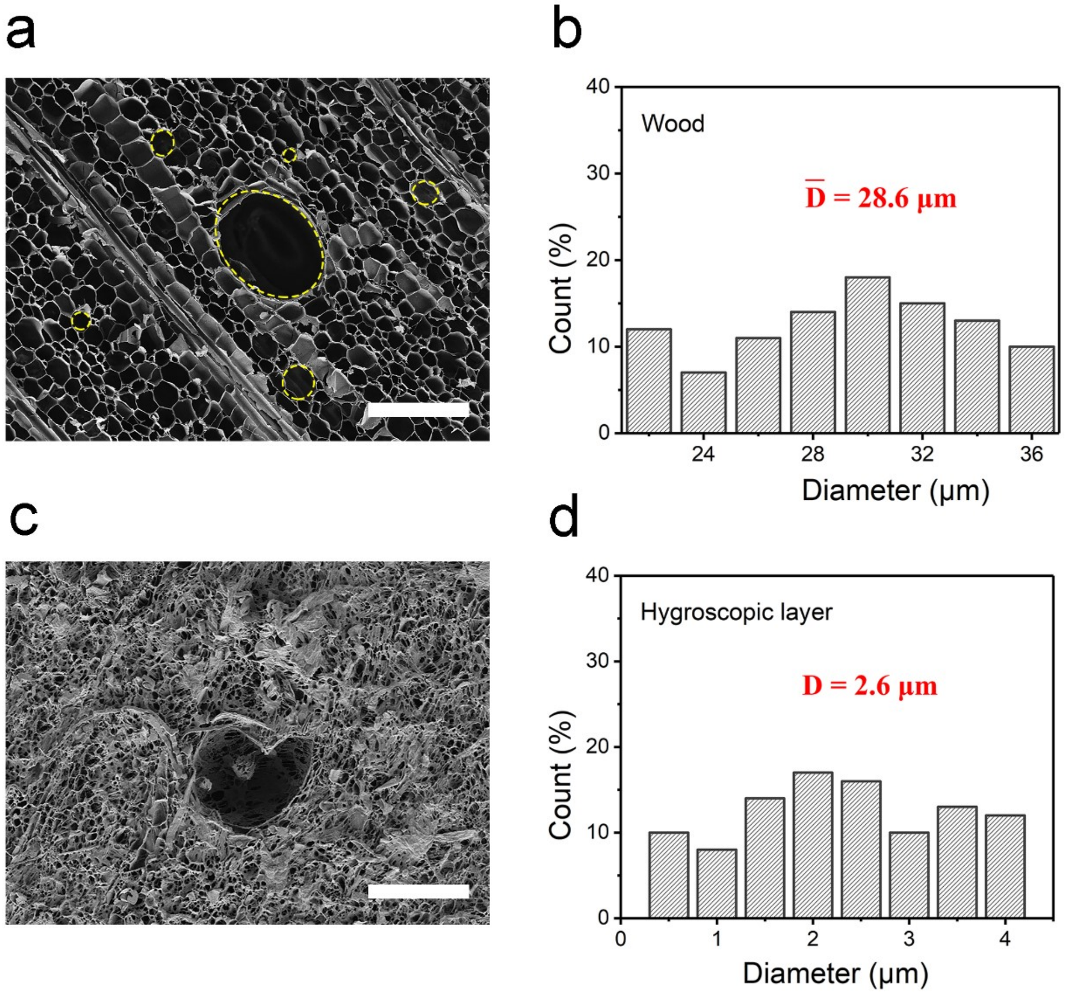


**Figure S2**. SEM images and pore size distribution statistics of (**a**, **b**) raw wood, and (**c**, **d**) wood-based ionic hydrogel. The scale is 50 μm.

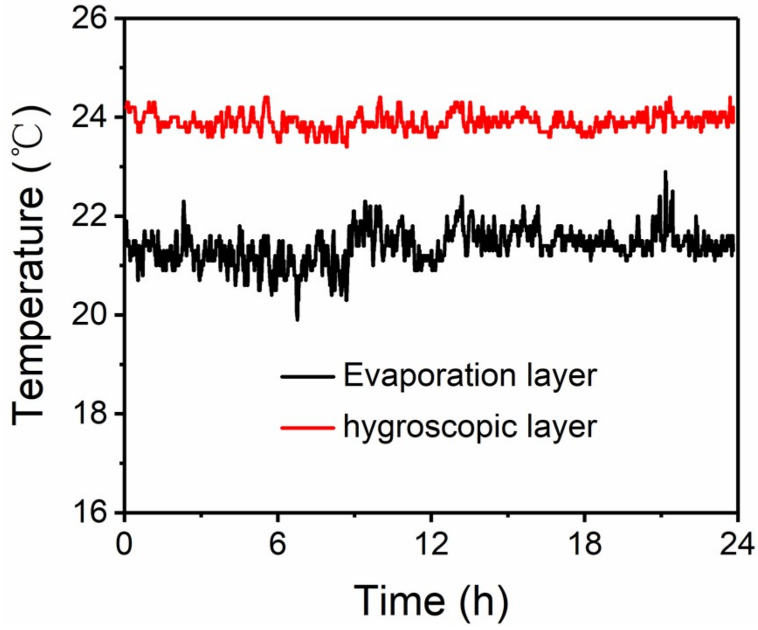


**Figure S3**. Real-time temperature detection of the evaporation and hygroscopic layers in natural environment.

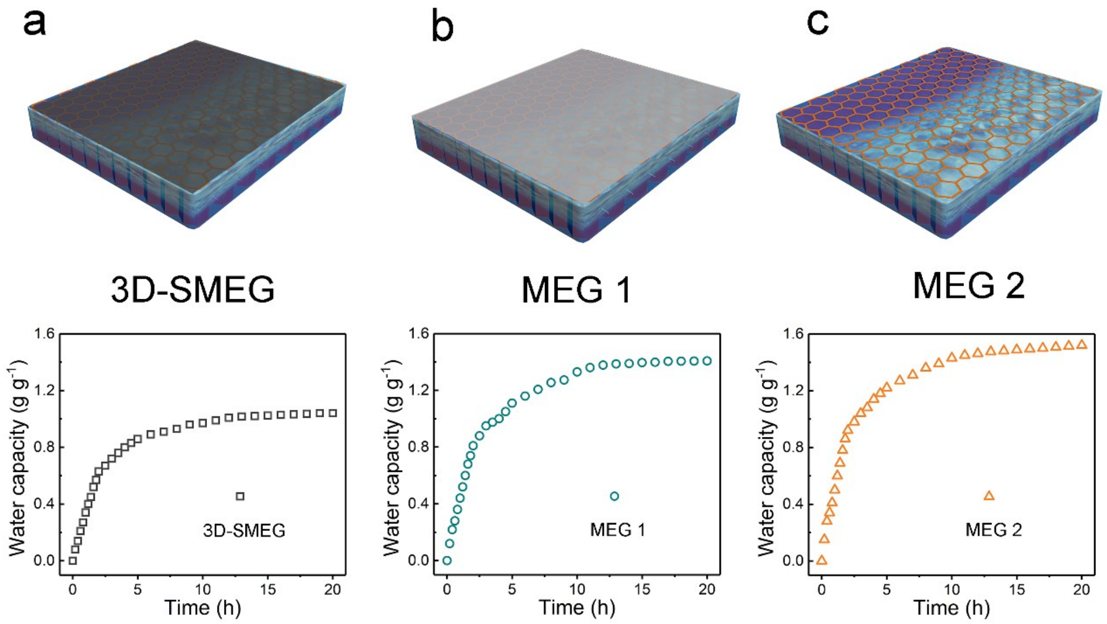


**Figure S4**. Comparison of hygroscopic properties of different devices at RH 60%, **a**. 3D-SMEG, **b**. MEG 1 is 3D-SMEG with evaporated layer encapsulated by epoxy resin, and **c**. MEG 2 is 3D-SMEG without CNT coating.

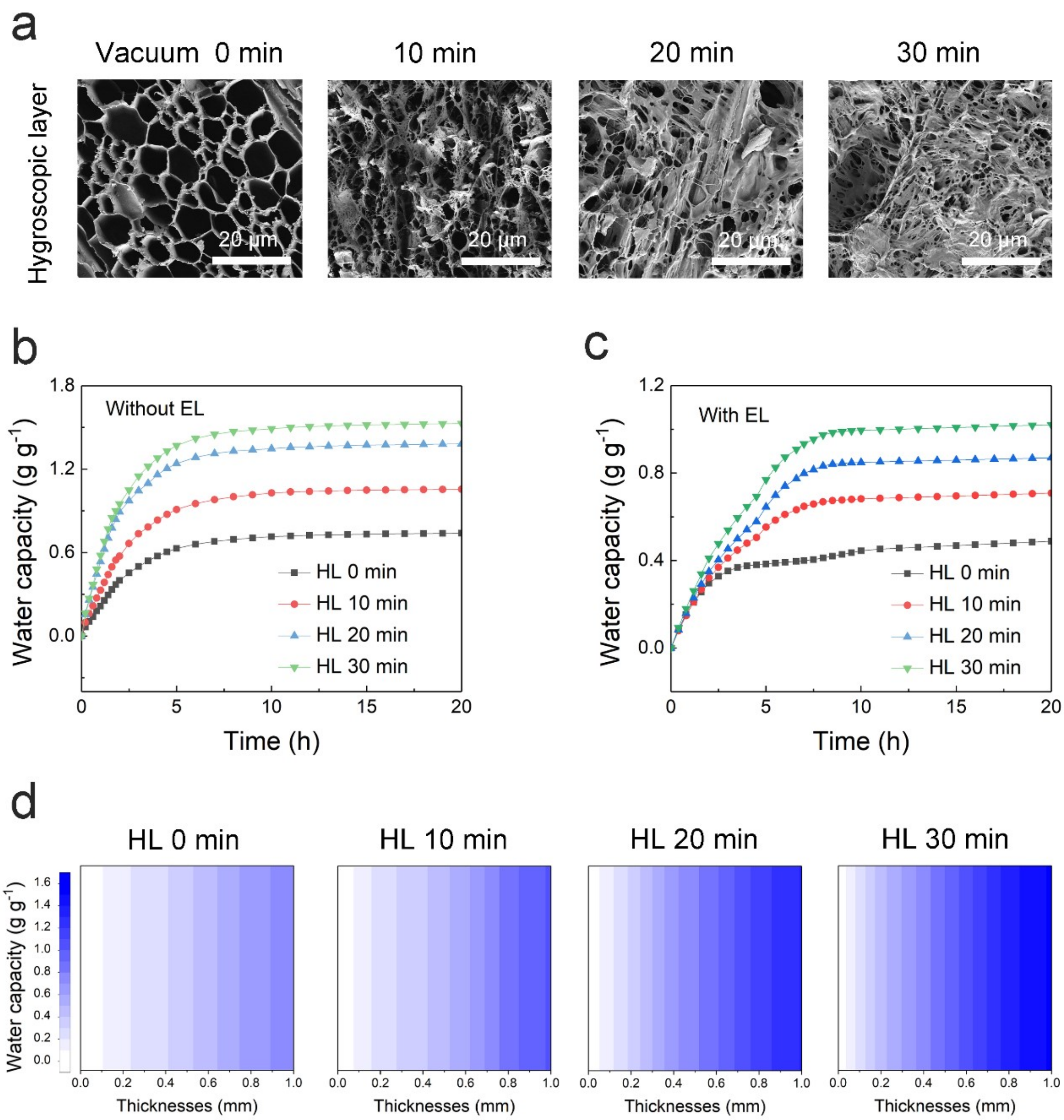


**Figure S5**. **a**. SEM images of the HLs fabricated with different vacuum treatment times. (0 min, 10 min, 20 min, and 30 min). **b**. Hygroscopic performance of the HLs measured at 60% RH. **c**. Hygroscopic performance of the bilayer structures (HL + EL), measured at 60% RH. **d**. Water content gradients of the 3D-SMEGs with different vacuum treatment times for the HL.

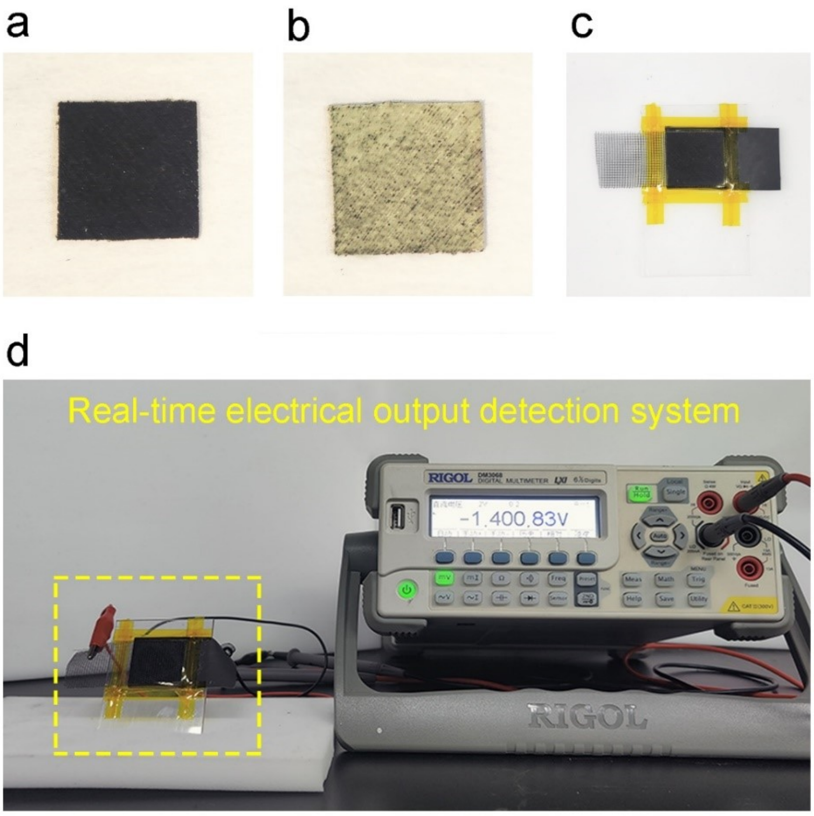


**Figure S6**. The photographs of **a**. evaporation layer, **b**. hygroscopic layer, **c**. 3D-SMEG, and **d**. real-time electrical output detection system.

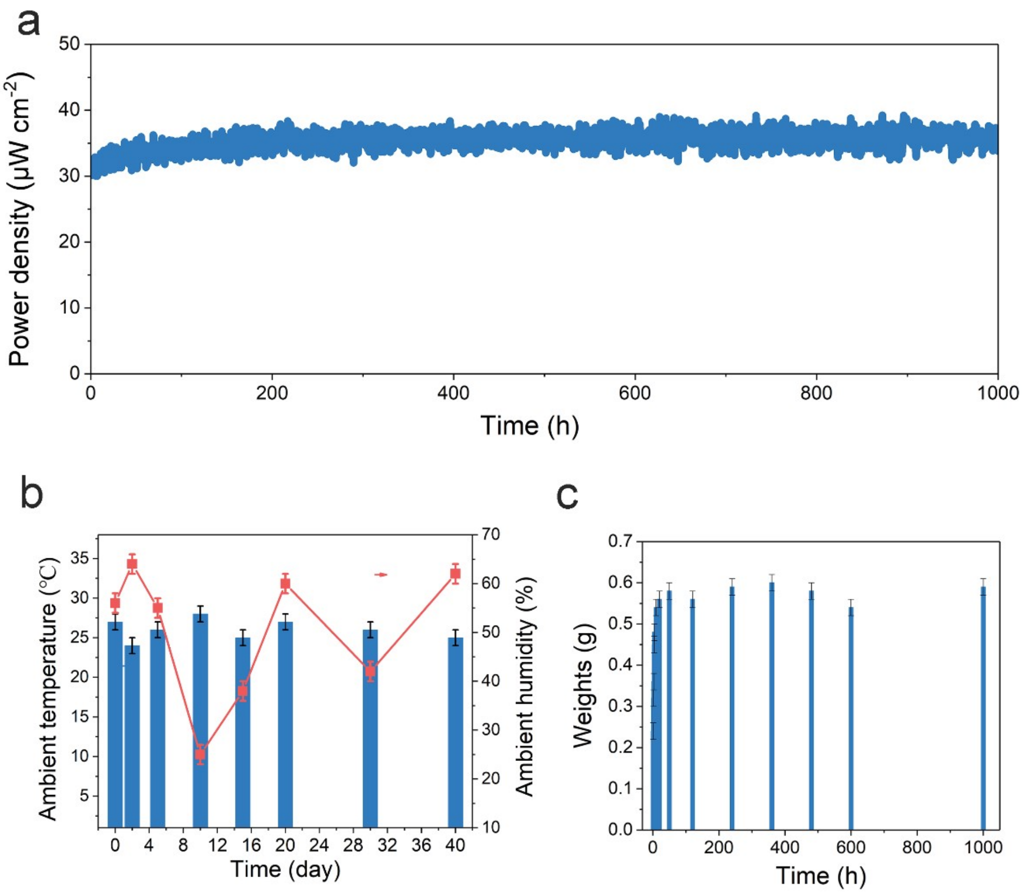


**Figure S7**. **a**. Recording of power density output, **b**. Ambient T/RH, and **c**. The weight of hydrogel film from the 3D-SMEG for 30 days in natural environment (20-28 °C, 25-70% RH).

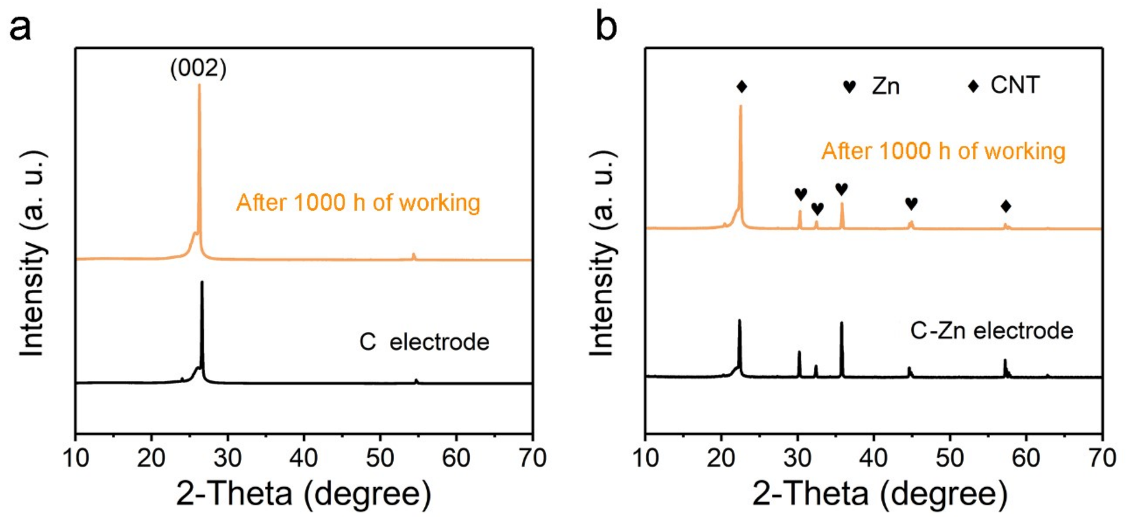


**Figure S8**. Comparison of XRD spectra of **a**. C, and **b**. C-Zn electrodes before and after 1000 hours of work.

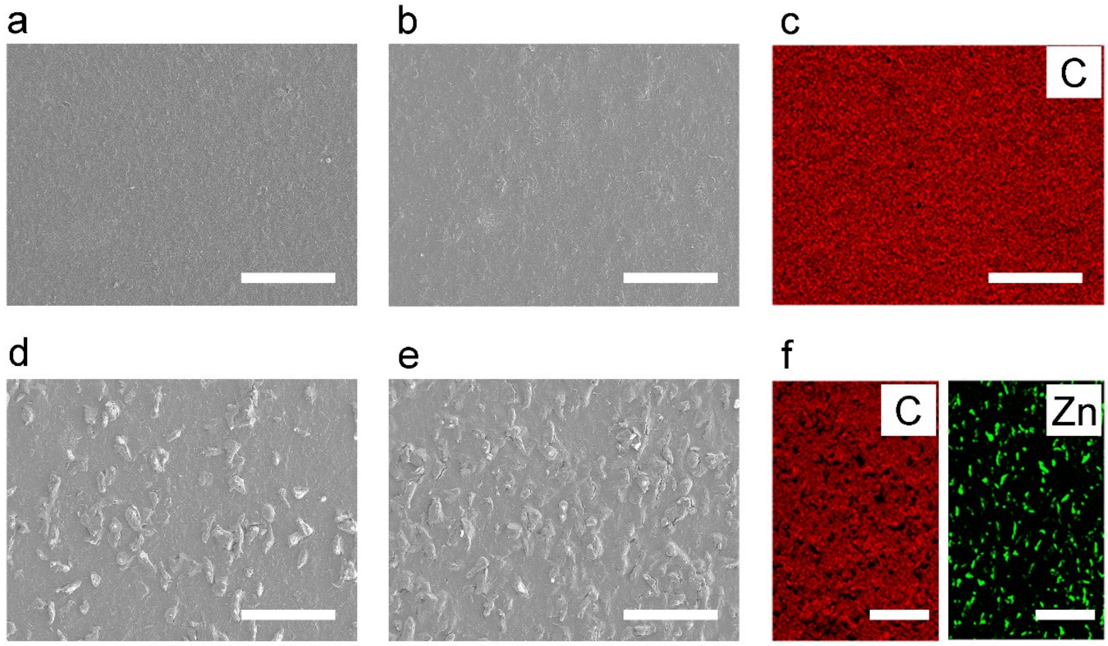


**Figure S9**. SEM images of **a**. C, and **d**. C-Zn electrodes before 30 days of work, **b**. C, and **e**. C-Zn electrodes after 30 days of work. **f**. EDX mapping of C, and C-Zn electrodes after 1000 hours of work.

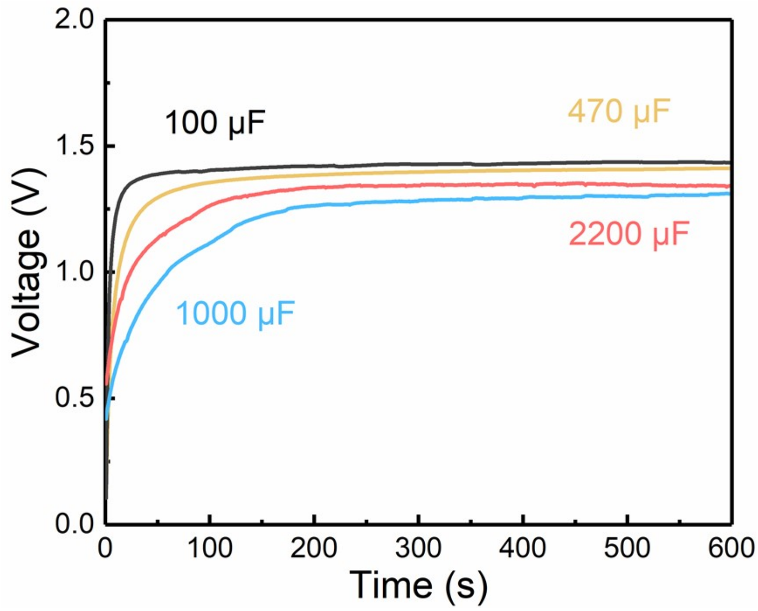


**Figure S10**. Real-time voltage variation of the 3D-SMEG powering a commercial capacitor.

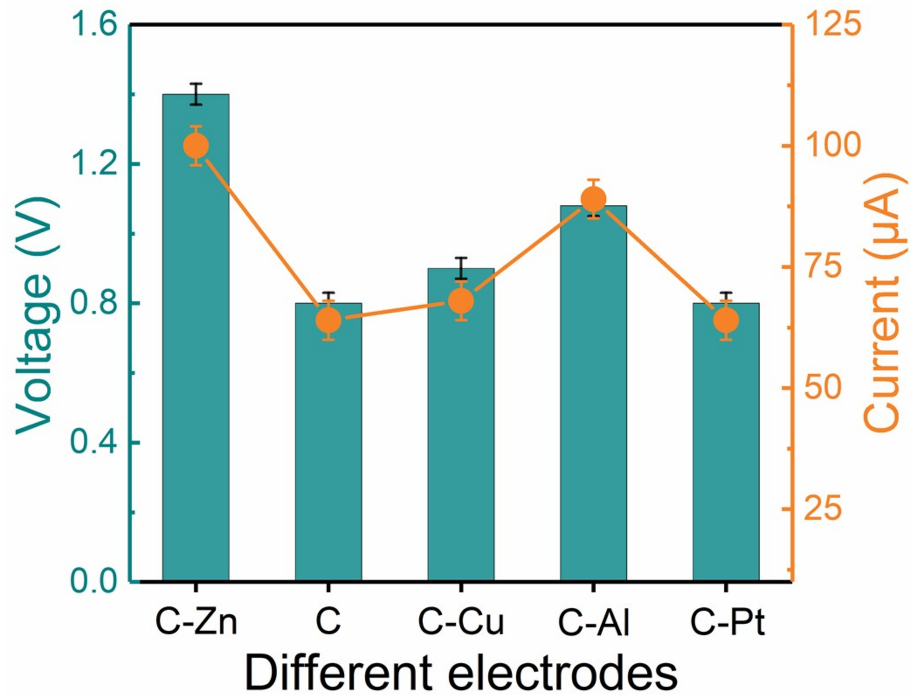


**Figure S11**. The electric output of 3D-SMEG with different negative electrodes including C-C, C-Zn, C-Al, C-Cu, and C-Pt.

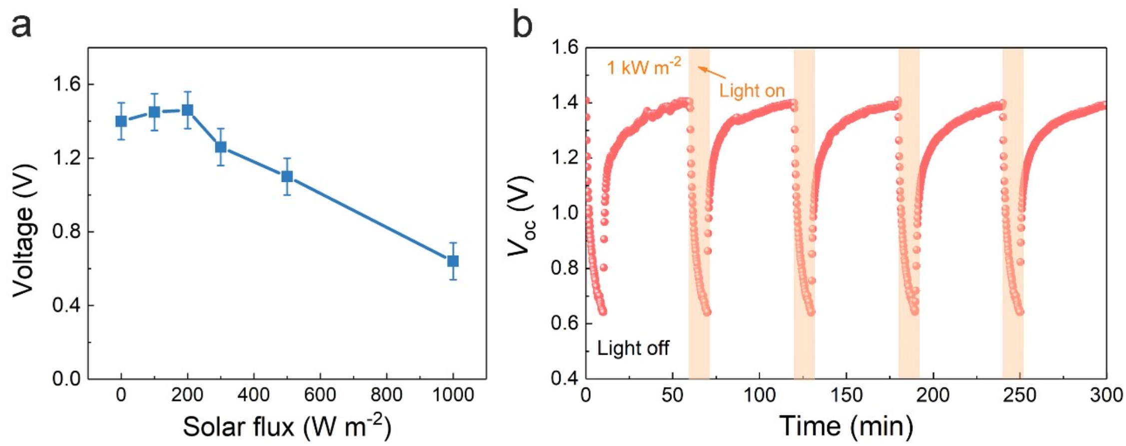


**Figure S12**. a. The $V_{oc}$ variation of 3D-SMEG under direct illumination with different light intensities. b. The $V_{oc}$ response of 3D-SMEG by vertically irradiating the evaporation layer with AM 1.5 illumination.

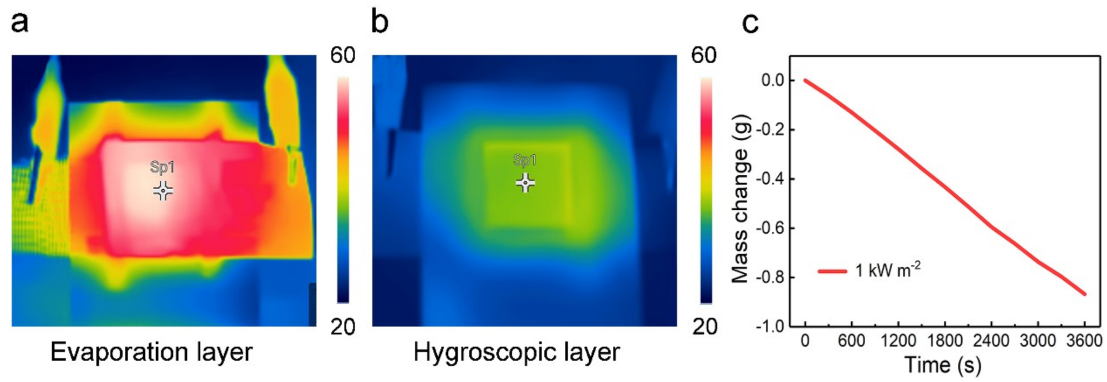


**Figure S13**. Infrared thermographic images of, **a**. evaporation layer, and **b**. hygroscopic layer of 3D-SMEG. **c**. The water desorption rate of 3D-SMEG by vertically irradiating the evaporation layer with AM 1.5 illumination.

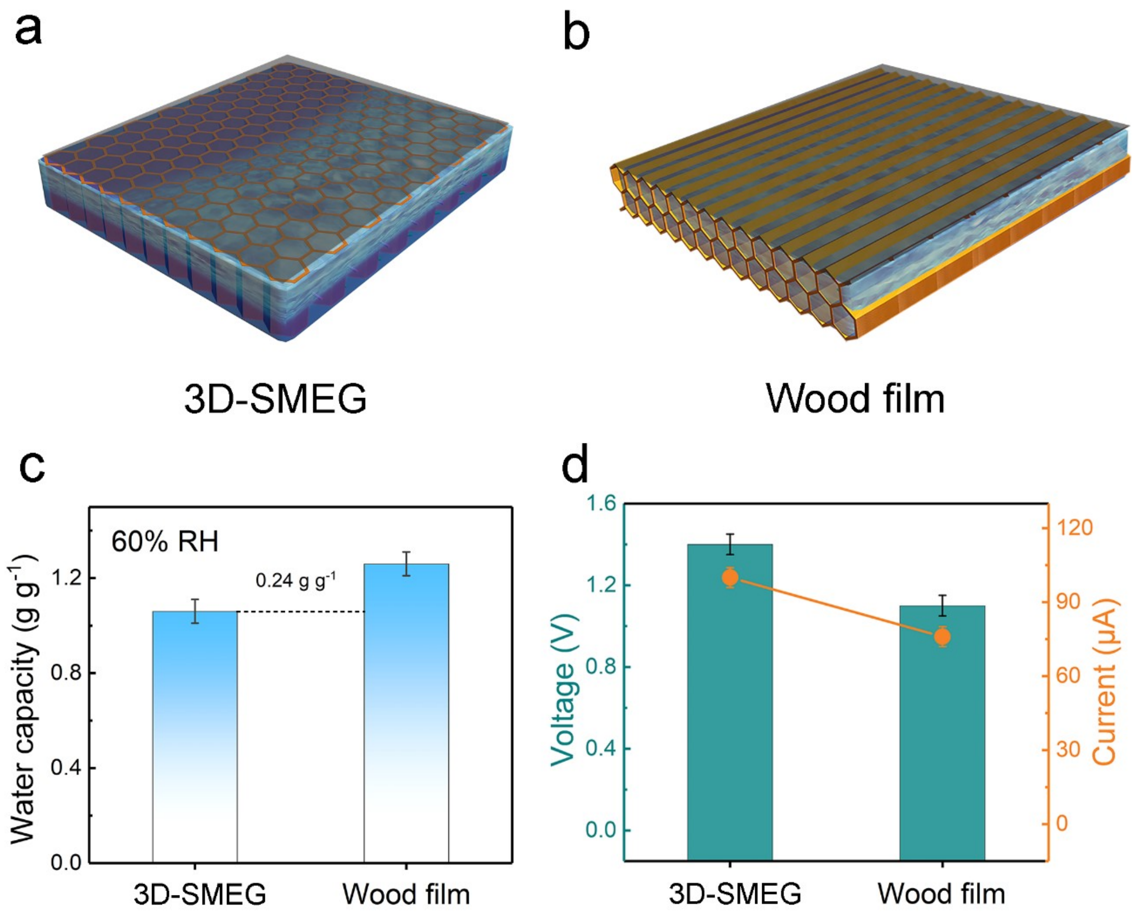


**Figure S14**. **a**. The structural characteristics of 3D-SMEG, **b**. MEG prepared using transverse wood film, **c**. the corresponding hygroscopic properties, and **d**. power generation performance.

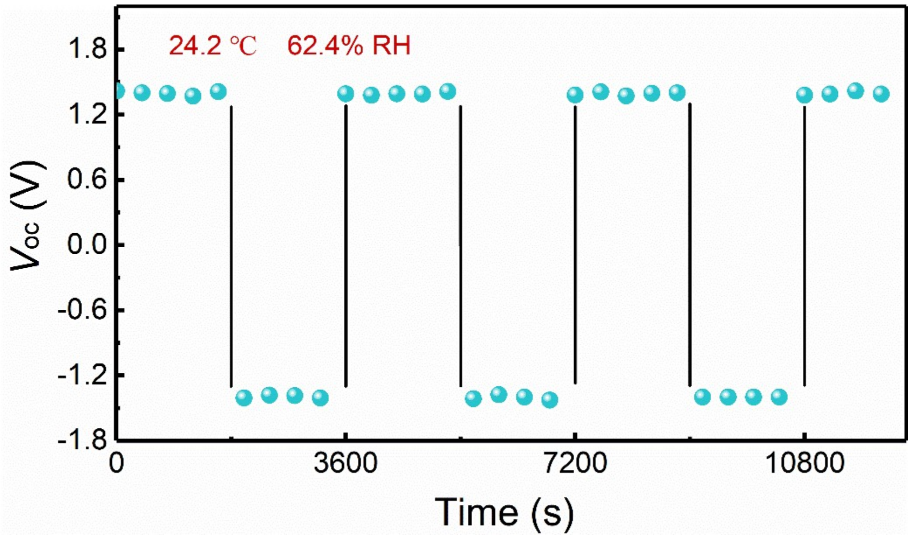


**Figure S15**. $V_{oc}$ was detected in real-time by repeatedly switching the connection mode between the 3D-SMEG and the electrostatic meter.

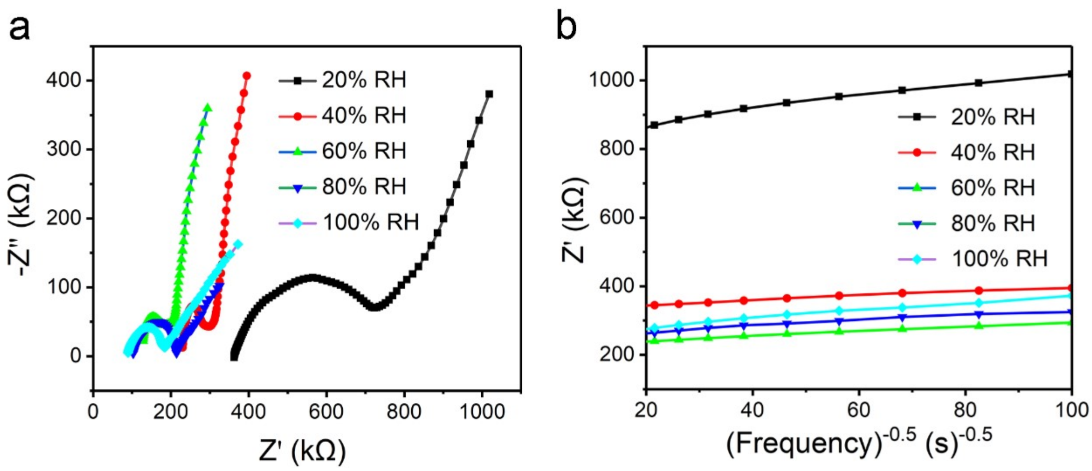


**Figure S16**. (**a**) Nyquist plots and (**b**) the corresponding relationship between Z′ and $\omega^{-0.5}$ in intermediate frequency region in different humidity environments.

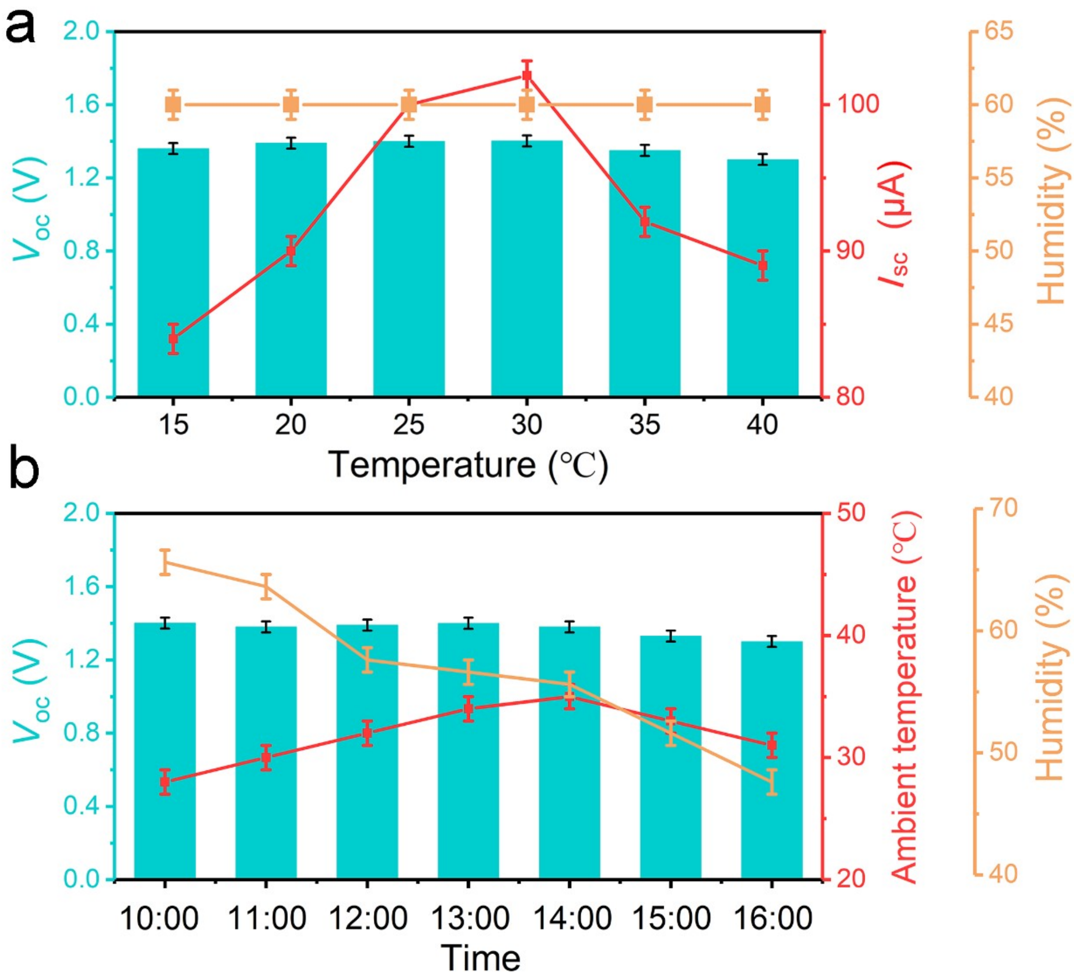


**Figure S17**. **a**. The electrical output performance of 3D-SMEG is tested in a constant humidity chamber at different temperatures. **b**. The variation of the electrical output performance of 3D-SMEG in real outdoor work.

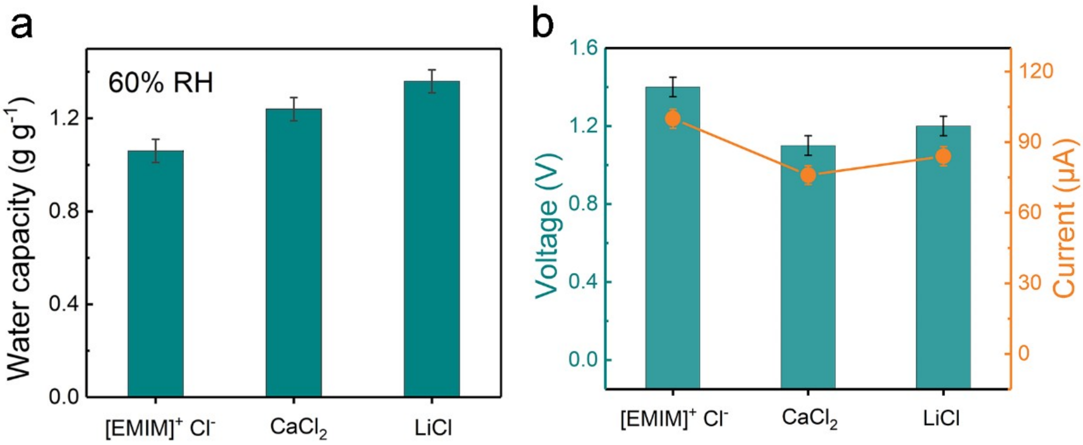


**Figure S18**. The water capacity (a) and electrical performance (b) of 3D-SMEG combined with hygroscopic salts of [EMIM$^+$] Cl$^-$, LiCl, and $CaCl_2$ in 60% RH.

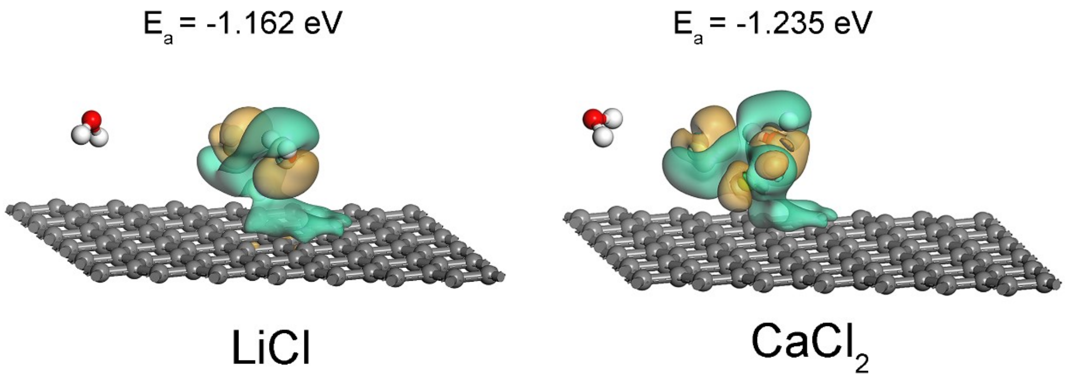


**F**

**igure S19**. Charge density difference plots for H adsorbed on CNT layer and the corresponding adsorption energy.

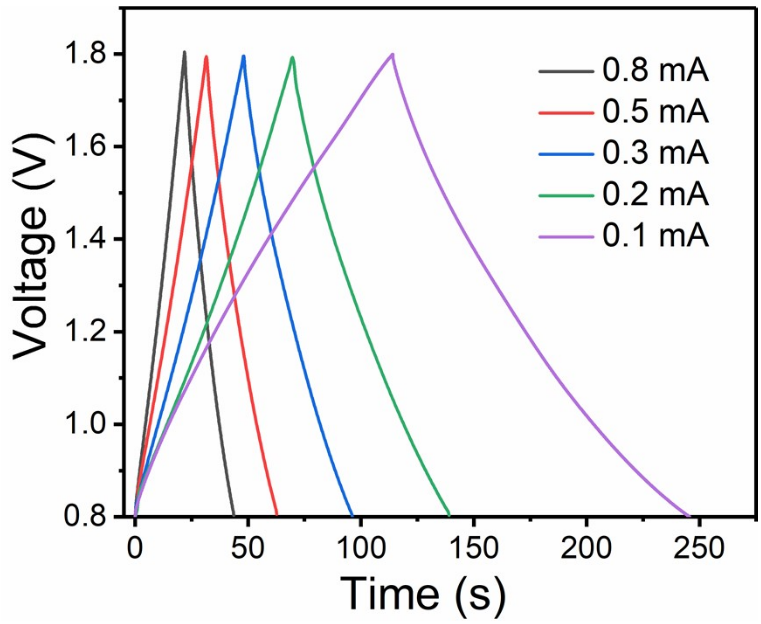


**Figure S20.** GCD curves of 3D-SMEG, indicating symmetric, linear curves at various currents.

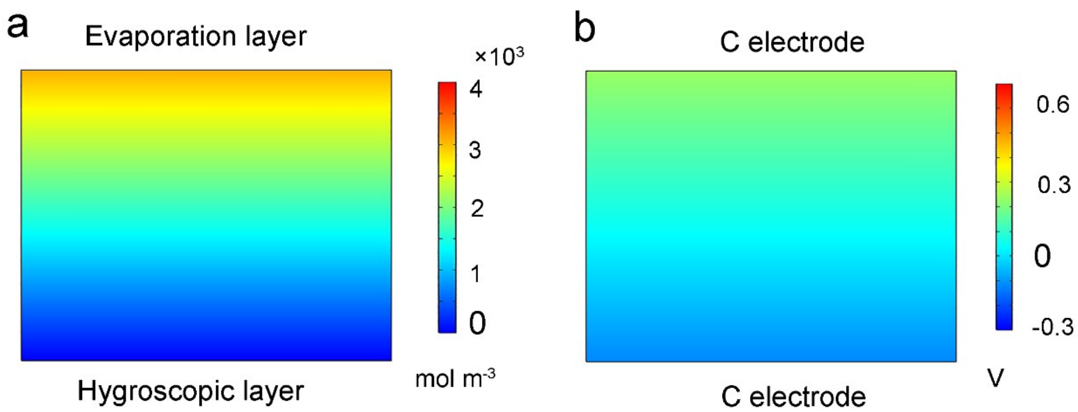


**Figure S21.** Numerical simulation of the correlative simulated ions-distribution profile for the evaporation and hygroscopic layer in 3D-SMEG, **a**. positive electric charge concentration distribution, and **b**. electric field distribution in the steady state.

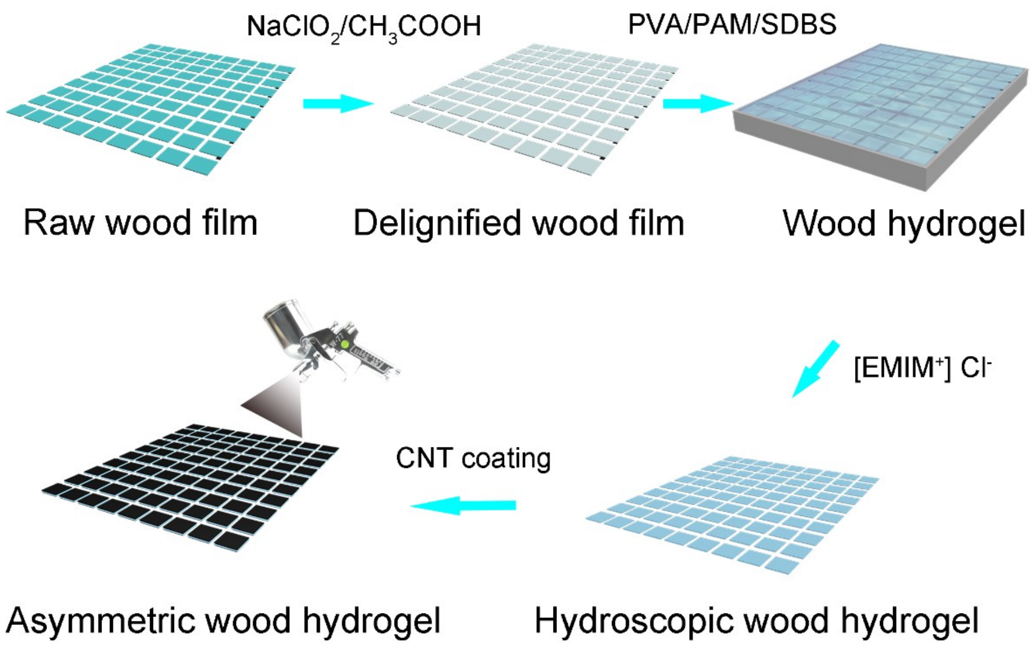


**Figure S22**. The batch preparation process of 3D-SMEG.

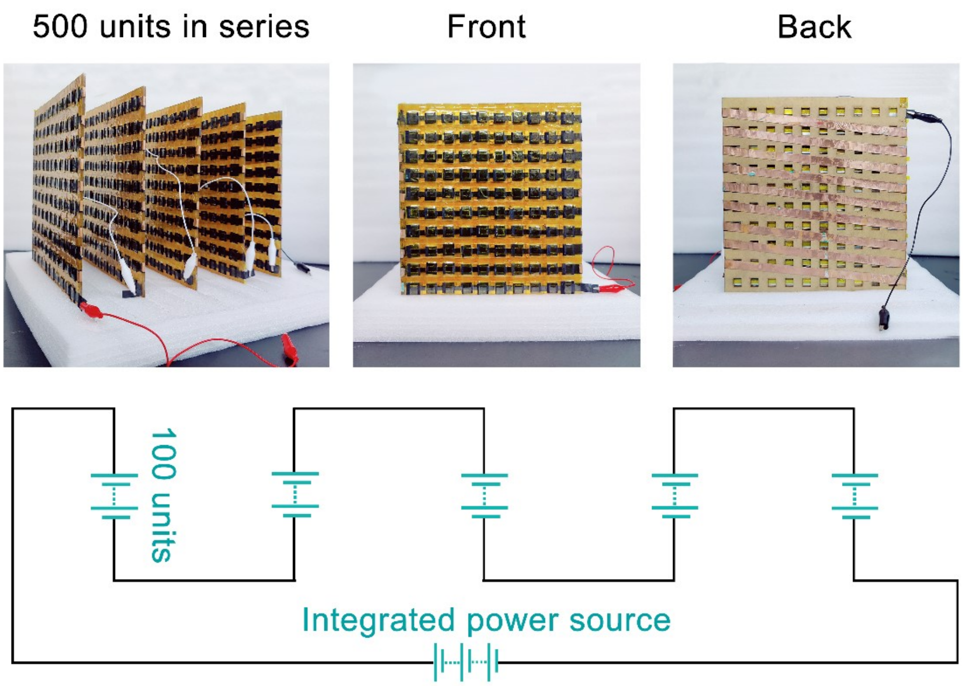


**Figure S23**. Optical photographs and circuit diagrams of the integrated self-powered system contains of 500 series-connected 3D-SMEGs for discharges.

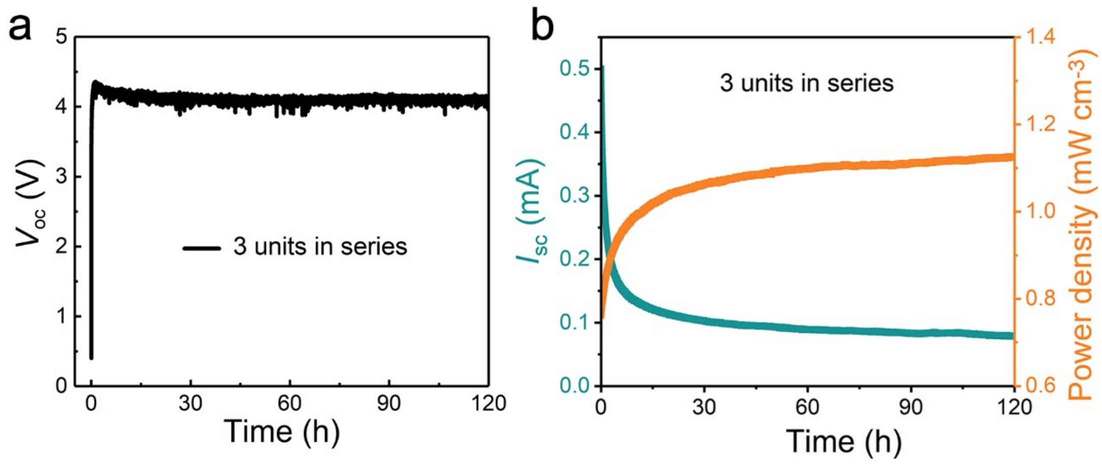


**Figure S24.** The $V_{oc}$, $I_{sc}$, and power density of the 3 series-connected 3D-SMEG units.

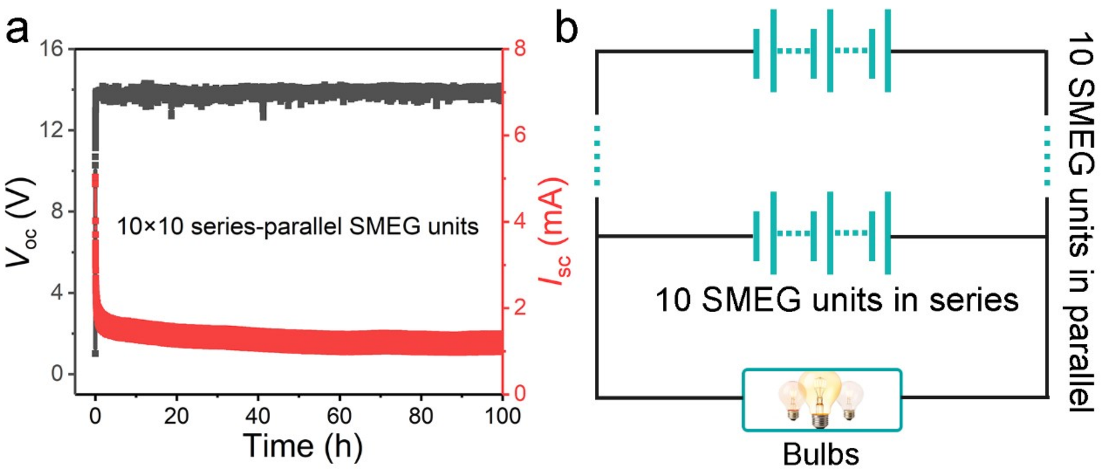


**Figure S25. a.** The $V_{oc}$, $I_{sc}$, and power density of the 10×10 series-parallel 3D-SMEG units and **b**. the corresponding circuit diagrams.

**Table S1:** Comparison of the power generation performance of 3D-SMEG with other reported MEGs.

| Reference | MEGs | $V_{oc}$/V | $I_{sc}$/μA | Power density/ μW cm$^{-2}$ |
|---|---|---|---|---|
| Ref 1 | BMEG | 1.02 | 3.16 | 1.06 |
| Ref 2 | HMEG | 1.38 | 6 | 5.52 |
| Ref 3 | mc-WEG | 0.3 | 50 | 0.7 |
| Ref 4 | Ionic diode–type | 1.1 | 7.7 | 1.3 |
| Ref 5 | PMEG | 1.1 | 11.3 | 2.6 |
| Ref 6 | SSEG | 0.78 | 7.5 | 0.16 |
| Ref 7 | $Al_2O_3$-MEG | 1.03 | 47.7 | 9.96 |
| Ref 8 | CMEG | 0.7 | 3 | 0.15 |
| Ref 9 | MEL | 0.28 | 1.8 | 0.12 |
| Ref 10 | MEG | 1.28 | 5.9 | 1.89 |
| Ref 11 | rMEC | 1.08 | 37 | 5.83 |
| **Avg.** | / | 0.84 | 15.09 | 2.44 |
| **This work** | **3D-SMEG** | **1.4** | **100 μA** | **35** |

**Table S2**: Comparison of the power generation performance between the integrated 3D-SMEG-based self-powered system and other reported MEG-based self-powered systems.

| Reference | $V_{oc}$/unit | Integrated numbers | $V_{oc}$ | Attrition rate/% |
|---|---|---|---|---|
| Ref 2 | 0.95 | 1600 | 1000 | 34.2 |
| Ref 5 | 1.1 | 200 | 200 | 9.1 |
| Ref 12 | 1.2 | 175 | 192 | 8.6 |
| Ref 13 | 0.8 | 300 | 180 | 25 |
| Ref 14 | 0.85 | 500 | 350 | 17.6 |
| Ref 15 | 1.3 | 50 | 62 | 4.6 |
| **This work** | **1.4** | **500** | **680** | **2.8** |

## References


1. Raktim G. et. al. Application of tandem heterojunction of metal oxides and hydroxides as robust and repairable moisture-electric generator. *Nano Energy* **131**, 110187 (2024).
2. Wang, H. et. al. Bilayer of polyelectrolyte films for spontaneous power generation in air up to an integrated 1,000 V output. *Nat. Nanotech.* **16**, 811–819. (2021)
3. Wen, X. et. al. High-performance fully stretchable moist-electric generator. *Adv. Funct. Mater.* **34**, 2311128 (2023).
4. Zhang, Y. et. al. Sustainable power generation for at least one month from ambient humidity using unique nanofluidic diode. *Nat. Commun.* **13**, 3484 (2022).
5. He, T. et. al. Fully printed planar moisture-enabled electric generator arrays for scalable function integration. *Joule* **7**, 935-951 (2023).
6. Tan, J. et. al. Self-sustained electricity generator driven by the compatible integration of ambient moisture adsorption and evaporation. *Nat. Commun.* **13**, 3643 (2022).
7. Yao Y. et. al. Patterned coating of ionic diode arrays toward flexible moist-electric generators to power wireless sensor nodes. *Adv. Funct. Mater.* **34**, 2311465 (2024).
8. Sun, Z. et. al. Capacitor-inspired high-performance and durable moist-electric

generator. *Energy Environ. Sci.* **15**, 4584-4591 (2022).
9. Duan, P. et. al. Moisture-based green energy harvesting over 600 hours via photocatalysis-enhanced hydrovoltaic effect, *Nat. Commun.* **16**, 239 (2025).
10. Duan, W. et. al. Silicon nanowire/ionic hydrogel-based hybrid moist-electric generators with enhanced voltage output and operational stability, *Energy Environ. Sci.*, **17**, 3788-3796 (2024).
11. Shi, M. et. al. Long cycle life rechargeable moisture-enabled electricity cell, *Adv. Energy Mater.* **14**, 2303815 (2024).
12. Yang, L. et. al. A moisture-enabled fully printable power source inspired by electric eels. *Proc. Natl. Acad. Sci.* **118**, e2023164118 (2021).
13. Huang, Y. et al. Three-dimensional printing of high-performance moisture power generators. *Adv. Funct. Mater.* **34**, 2308620 (2023).
14. Hu, Y. et al. Phyto-inspired sustainable and high-performance fabric generators via moisture absorption-evaporation cycles. *Sci. Adv.* **10**, eadk4620. (2024).
15. Su, Y. et al. Green moisture-electric generator based on supramolecular hydrogel with tens of milliamp electricity toward practical applications, *Nat. Commun.* **15**, 3329 (2024).